

24 necessity of precisely determining the effects of light-gated chloride channels under specific
25 experimental conditions and provide a much-improved light-gated chloride channel for
26 optogenetic inhibition.

27

28 **Introduction**

29 Targeted manipulation of neural activity is a powerful approach in neuroscience that has
30 provided fundamental insights into the roles of specific neurons in nervous system functions.
31 Genetically encoded actuators such as light-gated ion channels or pumps enable control of neural
32 activity with unprecedented spatiotemporal specificity and are transforming neuroscience
33 research (Boyden et al., 2005; Han and Boyden, 2007; Li et al., 2005; Nagel et al., 2003; Zhang
34 et al., 2007). Actuators that enable neuronal activation are frequently used, but inhibitory
35 optogenetic tools are increasingly crucial because reversible and temporally precise suppression
36 of neuronal activity is key to revealing the causal roles of specific neurons in network dynamics
37 and behavior. The widely used light-driven inward chloride pumps and outward proton pumps,
38 such as *Natronomonas pharaonis* halorhodopsin (NpHR) and *Halorubrum sodomense*
39 archaerhodopsin (Arch), can hyperpolarize membrane potentials, independent of the
40 electrochemical gradients, to inhibit action potentials with millisecond precision (Chow et al.,
41 2010; Chuong et al., 2014; Han and Boyden, 2007; Han et al., 2011; Zhang et al., 2007).
42 However, their efficacies are limited because only one ion is transported per absorbed photon,
43 and their activation does not decrease membrane resistance. Light-gated chloride channels, such
44 as *Guillardia theta* anion channelrhodopsin 1 and 2 (GtACR1 and GtACR2), iC⁺⁺, and iChloC,
45 overcome these limitations. They are highly sensitive to light, allow multiple ions to cross the
46 membrane per photocycle, and reduce membrane resistance, thereby potently inhibiting action

47 potentials (Berndt et al., 2014; Govorunova et al., 2015; 2017b; Wietek et al., 2014). Thus, light-
48 gated chloride channels are emerging as promising optogenetic tools for suppressing neuronal
49 activity (Govorunova et al., 2017a).

50

51 Determining the precise effects of light-gated ion channels or pumps under defined conditions is
52 a prerequisite to use them for interrogating the functions of specific neurons and circuits. This is
53 due to the possibility that these channels or pumps not only modulate membrane potentials but
54 also may affect other processes such as ion homeostasis or neurotransmitter release. For
55 example, activation of a light-driven inward chloride pump, eNpHR3.0, can transiently change
56 the reversal potential of GABA_A receptors and alter the inhibitory synaptic inputs (Raimondo et
57 al., 2012). Prolonged activation of a light-driven outward proton pump, eArch3.0, can increase
58 presynaptic calcium concentrations and spontaneous neurotransmitter release (Mahn et al.,
59 2016). Despite these potential confounds, these inhibitory optogenetic molecules are increasingly
60 essential tools for the targeted silencing of neuronal populations, as long as these confounds are
61 understood and controlled (Allen et al., 2015). Therefore, it is also crucial to thoroughly
62 characterize light-gated chloride channels, as their effect depends on the difference between the
63 membrane potential and the reversal potential for chloride, both of which can vary in different
64 neuronal types and subcellular compartments (Marty and Llano, 2005; Trigo et al., 2008).

65

66 To this end, we investigated the effects of activating GtACR2 in mouse cortical excitatory and
67 inhibitory neurons. Much to our surprise, wide-field light activation of GtACR2 not only
68 inhibited the soma, but also caused neurotransmitter release onto neighboring neurons. A similar
69 phenomenon was observed with GtACR1, iC⁺⁺, and iChloC. We further showed that GtACR2

70 activation in the axon and presynaptic terminals directly depolarized the membrane to induce
71 neurotransmitter release due to high chloride concentrations in these compartments. These data
72 explain the recent observations that photostimulation of neurons expressing GtACR1 or GtACR2
73 can paradoxically release neurotransmitters or generate action potentials (Mahn et al., 2016;
74 Malyshev et al., 2017). To reduce the excitatory effect of GtACR2, we screened a panel of
75 somatodendritic targeting motifs to reduce the trafficking of GtACR2 to the axon and
76 presynaptic terminals. We created a hybrid motif (Kv2.1C-linker-TlcnC) that is most effective in
77 concentrating GtACR2 in the somatodendritic domain. Activation of somatodendritically
78 targeted GtACR2 resulted in larger photocurrents at the soma and less neurotransmitter release
79 than wild type GtACR2. These results demonstrate that restricting localization of light-gated
80 chloride channels to the somatodendritic domain improves the inhibitory efficacy of these
81 optogenetic tools.

82

83 **Results**

84 **Light activation of GtACR2 in mouse cortical neurons causes neurotransmitter release**

85 To examine the efficacy of GtACR2 in mouse cortical excitatory neurons, we expressed a
86 GtACR2-EYFP fusion protein (referred to as GtACR2 below) together with a red fluorescent
87 protein, tdTomato, in layer 2/3 pyramidal neurons of the mouse visual or somatosensory cortex
88 by *in utero* electroporation of plasmids at embryonic day 14.5–15.5. We obtained acute coronal
89 brain slices from 3–8-week-old mice and observed that GtACR2 was present in the soma,
90 dendrites, and axon (**Figure 1A**). We performed whole-cell patch clamp recordings at the soma
91 of neurons expressing GtACR2 (GtACR2⁺ neurons) with a K⁺-based pipette solution (**Figure**
92 **1B**). As previously reported, activation of GtACR2 by wide-field blue light (455 nm) potently

93 inhibited current-induced spiking in these neurons (**Figure 1C**). However, when we voltage
94 clamped the neurons to record GtACR2-mediated photocurrents, we unexpectedly found an
95 inward current that was superimposed on the photocurrent. This inward current resembled an
96 excitatory postsynaptic current (EPSC; **Figure 1D**). To further investigate this phenomenon, we
97 recorded layer 2/3 pyramidal neurons that did not express GtACR2 (GtACR2⁻ neurons) with a
98 Cs⁺-based pipette solution (**Figure 1E**). GtACR2 activation generated inward currents in every
99 recorded GtACR2⁻ neuron that was voltage clamped at the reversal potential for GABAergic
100 inhibition (-60 mV). The onsets of these inward currents followed the onset of the blue light by
101 3.19 ± 0.26 ms (mean \pm s.e.m., $n = 25$). These currents were abolished by the glutamatergic
102 receptor antagonists, NBQX and CPP (**Figure 1F**), or the voltage-gated sodium channel blocker,
103 tetrodotoxin (TTX; **Figure 1G**), indicating that they were indeed monosynaptic EPSCs caused
104 by the glutamate transmitter released from GtACR2⁺ neurons. Activation of GtACR2 also
105 produced inhibitory postsynaptic currents (IPSCs) in GtACR2⁻ neurons that were voltage
106 clamped at the reversal potential for glutamatergic excitation (+10 mV). These IPSCs were
107 disynaptic because they were abolished by NBQX and CPP (**Figure 1-supplement 1**), indicating
108 that activating GtACR2 in pyramidal neurons can release sufficient glutamate to recruit
109 inhibitory interneurons.

110

111 To determine if the phenomenon of GtACR2-induced neurotransmitter release is also present in
112 inhibitory neurons, we expressed GtACR2 in parvalbumin-expressing (Pv) neurons by injecting
113 a Flpo recombinase-dependent adeno-associated virus (AAV) into the visual cortex of *Pvalb-2A-*
114 *Flpo* mice (*Pvalb*^{Flpo/+}) (Madisen et al., 2015) at postnatal day 1 (**Figure 1H**). Using acute brain
115 slices from 3–6-week-old mice, we found that activation of GtACR2 in Pv neurons generated

116 IPSCs in every recorded GtACR2⁻ layer 2/3 pyramidal neuron, and the IPSCs were abolished by
117 Gabazine, a GABA_A receptor antagonist, or TTX (*Figure 1I–K*). The onsets of the IPSCs
118 followed the onset of the blue light by 2.47 ± 0.15 ms (mean \pm s.e.m., $n = 17$), indicating that
119 they were monosynaptic IPSCs caused by the GABA transmitter released from GtACR2⁺ Pv
120 neurons. Furthermore, repetitive activation of GtACR2 in layer 2/3 pyramidal neurons or Pv
121 neurons with a high-frequency train of light pulses produced reliable EPSCs or IPSCs,
122 respectively (*Figure 1-supplement 2A,B*).

123

124 These findings were unexpected, because the Nernst equilibrium potential of chloride becomes
125 lower than the action potential threshold in rodent cortical neurons after the second postnatal
126 week, and activation of chloride channels should not promote neurotransmitter release onto
127 neighboring cells (Ben-Ari, 2002; Owens et al., 1996). We thus sought to identify the cause of
128 this paradoxical neurotransmitter release and considered three possibilities. First, GtACR2 may
129 conduct cations to depolarize neurons. Second, an increase in the intracellular chloride or strong
130 hyperpolarization induced by GtACR2 activation may lead to rebound spikes. Third, GtACR2-
131 mediated chloride currents may be excitatory.

132

133 **A GtACR2-mediated excitatory chloride conductance causes neurotransmitter release**

134 First, it was reported that GtACR2 did not conduct physiological cations (Govorunova et al.,
135 2015), but some other light-gated chloride channels retained certain cation conductance (Berndt
136 et al., 2014; Wietek et al., 2014). Thus, we sought to verify that in cortical neurons, GtACR2 has
137 a similar reversal potential as a known chloride channel. To accomplish this, we determined the
138 reversal potential of GtACR2-mediated photocurrents in comparison with that of IPSCs

139 mediated by the endogenous GABA_A receptors. We used *in utero* electroporation to express
140 GtACR2 in layer 2/3 pyramidal neurons and a Cre recombinase-dependent AAV to express a red
141 light-gated cation channelrhodopsin, ReaChR, in Pv neurons of *Pvalb-2A-Cre* mice (*Pvalb*^{Cre/+})
142 (Madisen et al., 2010). We performed whole-cell voltage clamp recordings at the soma of a
143 GtACR2⁺ layer 2/3 pyramidal neuron and a nearby GtACR2⁻ pyramidal neuron simultaneously
144 (**Figure 2-supplement 1A**). In the GtACR2⁺ neuron, we sequentially recorded the IPSCs induced
145 by activating ReaChR in Pv neurons via 617-nm light and the GtACR2-mediated photocurrents
146 activated by 455-nm light. Both IPSCs and photocurrents were recorded at different membrane
147 potentials to determine their reversal potentials in the same neuron (**Figure 2-supplement 1B,C**).
148 617-nm light does not activate GtACR2 (Govorunova et al., 2015), whereas 455-nm light
149 partially activates ReaChR (Lin et al., 2013). Thus, to avoid Pv neuron-mediated IPSCs
150 contaminating GtACR2-mediated photocurrents, we monitored the IPSCs in the GtACR2⁻
151 neuron at the membrane potential of +10 mV to ensure that the intensity of the 455-nm light was
152 not sufficient to activate Pv neurons and generate IPSCs (**Figure 2-supplement 1B**). We found
153 that the reversal potentials of GtACR2-mediated photocurrents and GABAergic IPSCs were
154 similar for each neuron and well below the action potential threshold (**Figure 2-supplement 1D**),
155 indicating that GtACR2 does not conduct cations to cause neurotransmitter release.
156
157 Second, we tested if GtACR2-induced neurotransmitter release could be due to rebound
158 depolarization. An increase in the intracellular chloride caused by GtACR2 activation may
159 trigger rapid efflux of chloride after the blue light illumination terminates. However, this
160 possibility is unlikely because when GtACR2 was activated by a long pulse of blue light (e.g., 5
161 ms), neurotransmitter release occurred before the light illumination ended (see examples in

162 **Figure 1F,G**). Another possibility is that the strong hyperpolarization induced by GtACR2
163 activates hyperpolarization-activated I_h currents, which may depolarize the membrane potential
164 above the action potential threshold. However, pharmacological inhibition of I_h currents slightly
165 increased the amplitudes of GtACR2-induced EPSCs (**Figure 2-supplement 2A,B**), most likely
166 because inhibiting I_h currents increases neuronal membrane resistances (Robinson and
167 Siegelbaum, 2003). Thus, GtACR2-induced neurotransmitter release is not caused by rebound
168 depolarization.

169

170 Third, although GtACR2-mediated photocurrents are inhibitory at the soma, it is possible that the
171 chloride concentrations are higher in some other cellular compartments, such that the
172 electrochemical gradient causes chloride to exit the cell upon GtACR2 channel opening,
173 resulting in depolarization of the membrane potential. To test this hypothesis, we
174 pharmacologically inhibited the activity of $\text{Na}^+ \text{-K}^+ \text{-2Cl}^-$ cotransporter 1 (NKCC1) with
175 bumetanide (50 or 100 μM) to decrease the intracellular chloride concentrations, as NKCC1 is
176 responsible for transporting chloride into neurons (Ben-Ari, 2017). When we activated GtACR2
177 in layer 2/3 pyramidal neurons, the resulting EPSCs in GtACR2⁻ pyramidal neurons were
178 diminished by bath application of bumetanide (**Figure 2A,B**), indicating that GtACR2-induced
179 neurotransmitter release requires high concentrations of intracellular chloride. An alternative
180 interpretation of this result would be that bumetanide blocks GtACR2 itself. To test this
181 possibility, we simultaneously recorded the photocurrents and EPSCs in GtACR2⁺ and GtACR2⁻
182 pyramidal neurons, respectively. While bumetanide diminished the EPSCs in GtACR2⁻ neurons,
183 it had no effect on the photocurrents in GtACR2⁺ neurons (**Figure 2-supplement 3A,B**), thereby
184 ruling out the possibility that bumetanide affects GtACR2 itself. Furthermore, when a cation

185 channel, channelrhodopsin-2 (ChR2) (Boyden et al., 2005; Li et al., 2005; Nagel et al., 2003),
186 was expressed and activated in layer 2/3 pyramidal neurons, the resulting EPSCs in ChR2⁻
187 neurons were not affected by bumetanide (**Figure 2C,D**), indicating that reducing the
188 intracellular chloride concentration only affects chloride-mediated, and not cation-mediated,
189 EPSCs. Finally, bumetanide also diminished the IPSCs resulting from GtACR2 activation in Pv
190 neurons (**Figure 2E,F**). Together, these results demonstrate that light activation of GtACR2
191 generates an excitatory chloride conductance in certain neuronal compartments to trigger
192 neurotransmitter release.

193

194 **Expression and activation of GtACR2 in adult neurons causes neurotransmitter release**

195 Since we expressed GtACR2 by *in utero* electroporation or neonatal AAV injection, we sought
196 to determine if the excitatory effect of GtACR2 was caused by the long-term expression of
197 GtACR2 throughout development that somehow altered the chloride homeostasis. To selectively
198 express GtACR2 in adult neurons, we *in utero* electroporated a Flpo-dependent plasmid into
199 layer 2/3 pyramidal neurons that will express GtACR2 only if Flpo is present (**Figure 2-**
200 **supplement 2C,D**). A Flpo-expressing AAV was then injected into the electroporated mice at
201 postnatal week 4 or 9 to turn on the GtACR2 expression. We obtained acute coronal brain slices
202 1–3 weeks after injecting Flpo-expressing AAV and found that light activation of GtACR2,
203 again, produced bumetanide-sensitive EPSCs in GtACR2⁻ neurons (**Figure 2-supplement 2E**).
204 Thus, it is unlikely that GtACR2 expression during neuronal development alters the chloride
205 homeostasis to render GtACR2 excitatory, as acute expression of GtACR2 in mature neurons
206 had the same effect.

207

208 **Activation of other light-gated chloride channels causes neurotransmitter release**

209 To determine if activation of other light-gated chloride channels can trigger neurotransmitter
210 release, we examined iC⁺⁺ and iChloC, two engineered blue light-gated chloride channels that
211 were converted from cation channelrhodopsins (Berndt et al., 2015; Wietek et al., 2015), and
212 GtACR1, another natural anion channelrhodopsin from *Guillardia theta* (Govorunova et al.,
213 2015). We *in utero* electroporated plasmids to express iC⁺⁺ in layer 2/3 pyramidal neurons of
214 the visual cortex and obtained acute coronal brain slices from 3–9-week-old mice. Similar to
215 GtACR2, light activation of iC⁺⁺ generated EPSCs in iC⁺⁺⁻ layer 2/3 pyramidal neurons that
216 were abolished by NBQX and CPP (amplitude reduced by $97.3 \pm 0.9\%$, mean \pm s.e.m., $n = 4$).
217 Bumetanide diminished the iC⁺⁺-induced EPSCs (**Figure 2G,H**) without affecting the iC⁺⁺-
218 mediated photocurrents (**Figure 2-supplement 3C,D**). We also expressed iC⁺⁺ in Pv neurons by
219 injecting a Cre-dependent AAV into *Pvalb*^{Cre/+} mice and found that light activation of iC⁺⁺
220 caused bumetanide-sensitive IPSCs in iC⁺⁺⁻ layer 2/3 pyramidal neurons (**Figure 2I,J**).
221 Similarly, when we expressed iChloC in Pv neurons, light activation of iChloC resulted in IPSCs
222 in 10 out of 17 recorded iChloC⁻ layer 2/3 pyramidal neurons (183 ± 42 pA, mean \pm s.e.m., $n =$
223 10), presumably because iChloC generated smaller photocurrents than iC⁺⁺ (iChloC, 292 ± 62
224 pA, $n = 7$; iC⁺⁺, 2182 ± 291 pA, $n = 15$; recorded at the membrane potential of +10 mV; mean \pm
225 s.e.m., $P < 0.0001$, *t*-test with Welch's correction). Finally, activation of GtACR1 in layer 2/3
226 pyramidal neurons produced EPSCs onto every recorded GtACR1⁻ pyramidal neuron (149 ± 47
227 pA, mean \pm s.e.m., $n = 11$). Altogether, these results demonstrate that activation of different
228 light-gated chloride channels in neurons can trigger neurotransmitter release.

229

230 **GtACR2 activation directly depolarizes the presynaptic terminals**

231 We hypothesized that the most likely neuronal compartments rendering GtACR2 excitatory were
232 the distal axon and presynaptic terminals because of the following previous findings. First,
233 activation of presynaptic GABA_A or glycine receptors enhanced neurotransmitter release at
234 several synapses of the hippocampus, cerebellum, and brainstem (Jang et al., 2006; Pugh and
235 Jahr, 2011; Stell et al., 2007; Turecek and Trussell, 2001). Second, the chloride concentrations
236 were 4–5 times higher in the presynaptic terminals of the Calyx of Held than the parent soma
237 (Price and Trussell, 2006). Third, there appeared to be an axo-somato-dendritic gradient in which
238 the reversal potentials of GABA from the axon to the soma and dendrites of cortical neurons
239 become progressively more negative (Khirug et al., 2008). To test our hypothesis, we expressed
240 GtACR2 in layer 2/3 pyramidal neurons of the visual cortex in one hemisphere as described
241 above and obtained acute coronal slices from the contralateral hemisphere (**Figure 3A**). GtACR2
242 was present in the long-range callosal projections in the contralateral hemisphere (**Figure 3-**
243 **supplement 1A**), which enabled us to activate GtACR2 in the axon and presynaptic terminals
244 that were severed from their parent somas. Light activation of GtACR2 in the callosal
245 projections generated EPSCs in layer 2/3 pyramidal neurons of the contralateral cortex, which
246 were diminished by TTX (**Figure 3-supplement 1B,C**) or bumetanide (**Figure 3B**). These results
247 demonstrate that activation of GtACR2 in the axon and presynaptic terminals is sufficient to
248 trigger neurotransmitter release.

249

250 If GtACR2-mediated chloride currents are excitatory in the presynaptic terminals, then GtACR2
251 should be similar to ChR2, whose activation can directly depolarize the presynaptic membrane in
252 the absence of action potentials to trigger neurotransmitter release (Petreanu et al., 2009). To test
253 this prediction, we recorded EPSCs or IPSCs in GtACR2⁻ neurons while activating GtACR2 in

254 layer 2/3 pyramidal neurons or Pv neurons, respectively (**Figure 3C,E**). As described above,
255 bath application of TTX abolished the EPSCs and IPSCs. However, when we further blocked
256 voltage-gated potassium channels by 4-aminopyridine (4-AP) and tetraethylammonium (TEA) to
257 prolong membrane depolarization (Petreanu et al., 2009), the EPSCs and IPSCs were partially
258 recovered (**Figure 3D,F**). These results indicate that in the absence of action potentials, light
259 activation of GtACR2 is sufficient to depolarize the presynaptic membrane to open voltage-gated
260 calcium channels and trigger neurotransmitter release.

261
262 We further tested if GtACR2-induced axonal depolarization could evoke antidromic action
263 potentials by performing extracellular loose-patch or whole-cell current clamp recordings at the
264 somas of GtACR2⁺ pyramidal neurons. We observed antidromic spikes in 9 out of 88 neurons
265 recorded in loose-patch configuration and 21 out of 56 neurons recorded in whole-cell
266 configuration in response to blue light stimulation (**Figure 3G,H**). In the whole-cell current
267 clamp recordings, although the chloride concentration in the patch pipette solution sets the
268 Nernst equilibrium potential of chloride around -85 mV (see Methods), blue light induced a
269 depolarization following the initial hyperpolarization. This observation is consistent with the
270 notion that the depolarization antidromically propagated from the distal axon to the soma
271 (**Figure 3H**). The antidromic spikes were not affected by NBQX and CPP, but were abolished by
272 TTX (**Figure 3H**), indicating that the spikes were generated within the GtACR2⁺ neurons, rather
273 than by excitatory inputs from other neurons. Antidromic spikes were only observed in a subset
274 of neurons, likely because the GtACR2 expression levels are heterogeneous in different neurons
275 and the hyperpolarization initiated at the soma can orthodromically propagate to counteract the
276 antidromic spikes. Similarly, TTX-sensitive antidromic spikes were observed in a subset of

277 GtACR2⁺ Pv neurons (3 out of 11 neurons in loose-patch configuration and 7 out of 17 neurons
278 in whole-cell configuration, **Figure 3I,J**). These results show that GtACR2-induced axonal
279 depolarization can be sufficient to elicit antidromic action potentials.

280

281 **Targeting GtACR2 to the somatodendritic domain reduces light-induced neurotransmitter** 282 **release**

283 Activating GtACR2 and other light-gated chloride channels inhibits the soma but depolarizes the
284 presynaptic terminals to release neurotransmitters. This dichotomic effect can confound the
285 utilization of these channels as inhibitory optogenetic tools for suppressing neuronal activity. We
286 reasoned that reducing the trafficking of light-gated chloride channels into the axon and
287 presynaptic terminals should reduce or eliminate their depolarizing action. Thus, we sought to
288 restrict GtACR2 within the somatodendritic domain of neurons by fusing GtACR2 with a
289 number of reported somatodendritic targeting motifs including a 26-amino acid Myosin Va-
290 binding domain of Melanophilin (MBD) (Lewis et al., 2009), a 32-amino acid cytoplasmic C-
291 terminal motif of Neuroligin 1 (Nlgn1C) (Rosales et al., 2005), a 16-amino acid dileucine-
292 containing motif of potassium channel Kv4.2 (Kv4.2LL) (Rivera et al., 2003), the N-terminal
293 150 residues of kainate receptor subunit 2 (KA2N) (Shemesh et al., 2017), the C-terminal 17
294 residues of Telencephalin (TlcnC) (Mitsui et al., 2005), and a 65-amino acid cytoplasmic C-
295 terminal motif of potassium channel Kv2.1 (Kv2.1C) (Lim et al., 2000). Each of these GtACR2
296 variants (**Figure 4-supplement 1**), along with tdTomato, were expressed in layer 2/3 pyramidal
297 neurons of the visual cortex by *in utero* electroporation (**Figure 4A**). Since GtACR2 was also
298 tagged with EYFP or EGFP, we compared the EYFP or EGFP fluorescence in layer 5, which
299 only contains the axons of layer 2/3 pyramidal neurons, with the EYFP or EGFP fluorescence in

300 layer 2/3 to estimate the distribution of GtACR2 between the axon and somatodendritic domain.
301 We normalized the EYFP or EGFP fluorescence ratio between layer 5 and layer 2/3 by the
302 tdTomato fluorescence ratio between layer 5 and layer 2/3 to control for variations in the
303 collateral axons. Among tested motifs, TlcnC and Kv2.1C were most effective in targeting
304 GtACR2 to the soma and dendrites (**Figure 4B**). As these two motifs may engage different
305 trafficking mechanisms, we combined them to create two hybrid motifs, Kv2.1C-TlcnC and
306 Kv2.1C-linker-TlcnC. Kv2.1C-linker-TlcnC turned out to be the best in restricting GtACR2
307 within the somatodendritic domain (**Figure 4A,B,C**). Interestingly, GtACR2-EYFP-Kv2.1C and
308 GtACR2-EYFP-Kv2.1C-linker-TlcnC showed less intracellular aggregation than wild type
309 GtACR2 (**Figure 4C**), suggesting that the somatodendritic targeting motifs also enhance the
310 surface expression of GtACR2. Finally, the EYFP fluorescence in the callosal projections in the
311 contralateral hemisphere was also reduced for GtACR2-EYFP-Kv2.1C-linker-TlcnC as
312 compared to GtACR2-EYFP (**Figure 4D,E**), demonstrating that Kv2.1C-linker-TlcnC decreased
313 the trafficking of GtACR2 into the distal axon.

314

315 To determine how targeting GtACR2 to the somatodendritic domain affects its photocurrent and
316 ability to trigger neurotransmitter release, we compared the somatodendritically targeted
317 GtACR2 variants, GtACR2-EYFP-Kv2.1C or GtACR2-EYFP-Kv2.1C-linker-TlcnC, with wild
318 type GtACR2 in the same litters of mice. We first recorded GtACR2⁺ layer 2/3 pyramidal
319 neurons and found that the blue light-activated photocurrents of GtACR2-EYFP-Kv2.1C or
320 GtACR2-EYFP-Kv2.1C-linker-TlcnC were 2.1- or 2.7-fold of GtACR2-EYFP photocurrents,
321 respectively (**Figure 5A–C**). We then recorded the EPSCs in GtACR2⁻ layer 2/3 pyramidal
322 neurons in response to different strengths of blue light stimulation. The EPSCs evoked by

323 activating GtACR2-EYFP-Kv2.1C or GtACR2-EYFP-Kv2.1C-linker-TlcnC were reduced by
324 52–60% or 65–77%, respectively, as compared to those evoked by activating GtACR2-EYFP
325 (**Figure 5D–H**). Furthermore, the EPSCs in layer 2/3 pyramidal neurons of the contralateral
326 cortex were reduced by 73% for GtACR2-EYFP-Kv2.1C-linker-TlcnC as compared to GtACR2-
327 EYFP when photostimulating the callosal projections (**Figure 5I,J**). These results show that the
328 somatodendritic targeting motifs, especially Kv2.1C-linker-TlcnC, shift GtACR2 from the axon
329 towards the soma and dendrites, thereby reducing the excitatory action in the axon and
330 presynaptic terminals while enhancing the inhibitory currents at the soma and dendrites.

331

332 **Discussion**

333 Optogenetic suppression of neuronal activity and synaptic outputs is an essential approach for
334 dissecting the roles of specific neurons in brain functions. Light-gated chloride channels,
335 particularly GtACR1 and GtACR2, are increasingly used due to their large photocurrents and
336 high sensitivity to light (Forli et al., 2018; Mardinly et al., 2018; Mauss et al., 2017; Mohamed et
337 al., 2017; Mohammad et al., 2017). To use these tools to their full potentials, it is necessary that
338 we understand their function and importantly, their limitations. The experiments here reveal that
339 wide-field activation of these channels in visual cortical neurons suppresses action potentials at
340 the soma but also triggers neurotransmitter release at the presynaptic terminals, therefore voiding
341 inhibition of neuronal activity. As demonstrated, the excitatory action of chloride channels is due
342 to the higher concentrations of chloride in the axon and presynaptic terminals relative to the
343 somatodendritic domain. However, it is worth noting that the heterogeneity of chloride gradients
344 across subcellular compartments may be cell-type dependent. For instance, gramicidin perforated
345 patch recordings from the axonal blebs of layer 5 pyramidal neurons in the prefrontal cortex of

346 rats revealed that the reversal potential of GABA_A receptors was more negative than the resting
347 membrane potential of the axon, which would indicate a hyperpolarizing effect of chloride
348 channels in this axon (Xia et al., 2014). Thus, it is critical to precisely determine the effect of
349 light-gated chloride channels, specific to each experimental design, when using them to
350 manipulate neuronal activity.

351

352 To create a better inhibitory optogenetic tool, we tested a number of somatodendritic targeting
353 motifs to confine GtACR2 in the soma and dendrites. We generated a hybrid motif, Kv2.1C-
354 linker-TlcnC, that was more effective than the widely used Kv2.1C (Baker et al., 2016; Mardinly
355 et al., 2018; Wu et al., 2013). The Kv2.1C motif was recently used in a bioRxiv preprint (Mahn
356 et al., 2017) to target GtACR2 to the somatodendritic domain. This GtACR2 variant achieved a
357 greater reduction of neurotransmitter release from the contralateral callosal projections of medial
358 prefrontal cortical neurons than what we observed with our GtACR2-EYFP-Kv2.1C and
359 GtACR2-EYFP-Kv2.1C-linker-TlcnC in visual cortical neurons. This quantitative difference is
360 likely due to different expression levels, light stimulation strengths, and neuronal types, which
361 reiterates the importance of characterizing the specific effect of light-gated chloride channels for
362 a given experiment.

363

364 Although the excitatory effect of light-gated chloride channels is undesired for neuronal
365 silencing, a potential utilization of their dual actions at the presynaptic terminals and soma is to
366 activate specific projections of neurons while minimizing the effect of antidromic spikes. For
367 example, long-range projection neurons often target multiple brain areas, and sometimes it is
368 desired to selectively excite the axonal terminals projecting to one particular area. If ChR2 is

369 used, local activation of ChR2-expressing axonal terminals may generate antidromic spikes,
370 which will affect other projections (Kim et al., 2017). However, if GtACR2 is used, one can
371 simultaneously activate GtACR2 in the soma and axonal terminals. Axonal depolarization will
372 result in neurotransmitter release, but the antidromic spikes will be reduced or suppressed by the
373 hyperpolarization originating from the somatodendritic domain, which reduces the likelihood of
374 activating other projections.

375

376 While GtACR2-EYFP-Kv2.1C-linker-TlcnC can still traffic to the axon to cause
377 neurotransmitter release, it is thus far the most improved light-gated chloride channel for
378 optogenetic inhibition. Since it can generate much larger photocurrents in the somatodendritic
379 domain than what is necessary to suppress action potentials, one approach to use this tool is to
380 reduce the overall GtACR2 expression level to further decrease its presence in the axon while
381 generating sufficient inhibitory photocurrents at the soma. Another approach is to selectively
382 photostimulate GtACR2 at the soma by two-photon excitation (Forli et al., 2018; Mardinly et al.,
383 2018). However, it is difficult to apply this photoactivation approach to freely moving animals or
384 deep brain areas. Therefore, it is imperative that we further engineer the channels to eliminate
385 their excitatory action in the axonal terminals. Future strategies include generating more
386 effective somatodendritic targeting motifs, creating outwardly rectifying channels, and the
387 combination of both strategies. The GtACR2-EYFP-Kv2.1C-linker-TlcnC reported here will
388 serve as the foundation for future improvement, which will enhance the available toolkit for
389 optogenetic inhibition.

390

391 **Materials and methods**

392 **Mice**

393 All procedures to maintain and use mice were approved by the Institutional Animal Care and
394 Use Committee at Baylor College of Medicine. Mice were maintained on 14-h:10-h light:dark
395 cycle with regular mouse chow and water ad libitum. Experiments were performed during the
396 light cycle. ICR female mice were purchased from Baylor College of Medicine Center for
397 Comparative Medicine or Charles River Laboratories. C57BL6/J, *Pvalb-2A-Cre*, and *Pvalb-2A-*
398 *Flpo* mice were obtained from Jackson Laboratory (stock numbers 000664, 012358, and 022730,
399 respectively). Both male and female mice were used in the experiments. The mice were used at
400 the age of 3–9 weeks for experiments, except for the conditional expression of GtACR2 in
401 adults, where mice were used at the age of 10–12 weeks.

402

403 **DNA constructs**

404 Plasmids pLenti-UbiC-GtACR2-EYFP (Addgene #67877) and pLenti-UbiC-GtACR1-EYFP
405 (Addgene #67795) were obtained from Dr. John Spudich, pAAV-CaMKII α -iC $^{++}$ -TS-EYFP and
406 pAAV-EF1 α -DIO-iC $^{++}$ -TS-EYFP from Dr. Karl Deisseroth, pAAV-EF1 α -DIO-iChloC-T2A-
407 mCherry from Drs. Matthew Caudill and Massimo Scanziani, pCAG-tdTomato from Anirvan
408 Ghosh, and pCAG-Cre from Addgene (#13775). Plasmid pCAG-Flpo (Addgene #60662) was
409 previously described (Xue et al., 2014). pCAG-hChR2(H134R)-EYFP was created by replacing
410 the EGFP in pCAG-EGFP (Addgene #11150) with the hChR2(H134R)-EYFP from pAAV-
411 EF1 α -DIO-hChR2(H134R)-EYFP (Addgene #20298). pAAV-EF1 α -DIO-ReaChR-P2A-
412 dTomato was created by replacing the oChIEF(E163A T199C) in pAAV-EF1 α -DIO-
413 oChIEF(E163A T199C)-P2A-dTomato (Addgene #51094) with the ReaChR from pAAV-hSyn-
414 FLEX-ReaChR-Citrine (Addgene #50955). pAAV-EF1 α -FRT-FLEX-GtACR2-EYFP and

415 pAAV-EF1 α -FRT-FLEX-GtACR1-EYFP were created by replacing the mNaChBac-T2A-
416 tdTomato in pAAV-EF1 α -FRT-FLEX-mNaChBac-T2A-tdTomato (Addgene #60658) with the
417 GtACR2-EYFP and GtACR1-EYFP from pLenti-UbiC-GtACR2-EYFP and pLenti-UbiC-
418 GtACR1-EYFP, respectively. Motifs MBD, Nlgn1C, Kv4.2LL, TlcnC, Kv2.1C, Kv2.1C-TlcnC,
419 and Kv2.1C-linker-TlcnC (see **Figure 4-supplement 1**) were generated by PCR and added to the
420 C-terminus of the GtACR2-EYFP to create pAAV-EF1 α -FRT-FLEX-GtACR2-EYFP-MBD,
421 pAAV-EF1 α -FRT-FLEX-GtACR2-EYFP-Nlgn1C, pAAV-EF1 α -FRT-FLEX-GtACR2-EYFP-
422 Kv4.2LL, pAAV-EF1 α -FRT-FLEX-GtACR2-EYFP-TlcnC, pAAV-EF1 α -FRT-FLEX-
423 GtACR2-EYFP-Kv2.1C, pAAV-EF1 α -FRT-FLEX-GtACR2-EYFP-Kv2.1C-TlcnC, and pAAV-
424 EF1 α -FRT-FLEX-GtACR2-EYFP-Kv2.1C-linker-TlcnC, respectively. pAAV-EF1 α -FRT-
425 FLEX-GtACR2-KA2N-EGFP was created by replacing the EYFP in pAAV-EF1 α -FRT-FLEX-
426 GtACR2-EYFP with the KA2N-EGFP from pAAV-hSyn-soCoChR-EGFP (Addgene #107708,
427 obtained from Dr. Edward Boyden).

428

429 ***In utero* electroporation**

430 Female ICR mice were crossed with male C57BL6/J, *Pvalb-2A-Cre*, or *Pvalb-2A-Flpo* mice to
431 obtain timed pregnancies. *In utero* electroporation was performed as previously described (Xue
432 et al., 2014) with a square-wave pulse generator (Gemini X2, BTX Harvard Bioscience). To
433 express GtACR2, GtACR1, iC⁺⁺, or ChR2 in layer 2/3 pyramidal neurons, pLenti-UbiC-
434 GtACR2-EYFP, pLenti-UbiC-GtACR1-EYFP, pAAV-CaMKII α -iC⁺⁺-TS-EYFP, or pCAG-
435 hChR2(H134R)-EYFP (all 2 μ g/ μ l) was used, respectively. In a few experiments, pAAV-EF1 α -
436 FRT-FLEX-GtACR2-EYFP (2 μ g/ μ l) with pCAG-Flpo (0.2 μ g/ μ l), pAAV-EF1 α -FRT-FLEX-
437 GtACR1-EYFP (2 μ g/ μ l) with pCAG-Flpo (0.2 μ g/ μ l), or pAAV-EF1 α -DIO-iC⁺⁺-TS-EYFP (2

438 $\mu\text{g}/\mu\text{l}$) with pCAG-Cre ($0.2 \mu\text{g}/\mu\text{l}$) was used to express GtACR2, GtACR1, or iC++,
439 respectively. To express somatodendritically targeted GtACR2 variants in layer 2/3 pyramidal
440 neurons and compare them with wild type GtACR2, the pAAV-EF1 α -FRT-FLEX constructs
441 described above were used (all $2 \mu\text{g}/\mu\text{l}$) with pCAG-Flpo ($0.2 \mu\text{g}/\mu\text{l}$). pCAG-tdTomato
442 ($0.1 \mu\text{g}/\mu\text{l}$) was included in all experiments. The plasmid concentrations stated above were final
443 concentrations in the plasmid mix. Transfected pups were identified by the transcranial
444 fluorescence of tdTomato with a MZ10F stereomicroscope (Leica) 1–2 days after birth.

445

446 **AAV production and injection**

447 All recombinant AAV serotype 9 vectors were produced by the Baylor College of Medicine
448 Gene Vector Core except AAV9-hSyn-Flpo (Addgene #60663), which was produced by the
449 Penn Vector Core and was previously described (Xue et al., 2014). To express GtACR2,
450 ReaChR, iC++, or iChloC in Pv neurons, 200–250 nl of the following recombinant AAV
451 serotype 9 vectors at their respective titer were injected into the visual cortex of *Pvalb*^{Flpo/+} (for
452 GtACR2) or *Pvalb*^{Cre/+} (for ReaChR, iC++, or iChloC) mice at postnatal day 1 as previously
453 described (Xue et al., 2014): AAV9-EF1 α -FRT-FLEX-GtACR2-EYFP (3.8×10^{13} genome
454 copies/ml), AAV9-EF1 α -DIO-ReaChR-P2A-dTomato (7.0×10^{13} genome copies/ml), AAV9-
455 EF1 α -DIO-iC++-TS-EYFP (3.71×10^{13} genome copies/ml), and AAV9-EF1 α -DIO-iChloC-2A-
456 mCherry (3.7×10^{14} genome copies/ml). To conditionally express GtACR2 in juvenile and adult
457 neurons, mice previously electroporated with plasmid pAAV-EF1 α -FRT-FLEX-GtACR2-EYFP
458 into layer 2/3 pyramidal neurons were injected with 200 nl of AAV9-hSyn-Flpo (1.2×10^{12}
459 genome copies/ml) at postnatal day 23, 60, or 64. Injection was performed as previously
460 described (Xue et al., 2014) with an UltraMicroPump III and a Micro4 controller (World

461 Precision Instruments).

462

463 **Brain slice electrophysiology**

464 Mice were anesthetized by an intraperitoneal injection of a ketamine and xylazine mix (80 mg/kg
465 and 16 mg/kg, respectively) and transcardially perfused with cold (0–4°C) slice cutting solution
466 containing 80 mM NaCl, 2.5 mM KCl, 1.3 mM NaH₂PO₄, 26 mM NaHCO₃, 4 mM MgCl₂, 0.5
467 mM CaCl₂, 20 mM D-glucose, 75 mM sucrose and 0.5 mM sodium ascorbate (315 mosmol, pH
468 7.4, saturated with 95% O₂/5% CO₂). Brains were removed and sectioned in the cutting solution
469 with a VT1200S vibratome (Leica) to obtain 300-μm coronal slices. Slices were incubated in a
470 custom-made interface holding chamber saturated with 95% O₂/5% CO₂ at 34 °C for 30 min and
471 then at room temperature for 20 min to 10 h until they were transferred to the recording chamber.
472 Recordings were performed on submerged slices in artificial cerebrospinal fluid (ACSF)
473 containing 119 mM NaCl, 2.5 mM KCl, 1.3 mM NaH₂PO₄, 26 mM NaHCO₃, 1.3 mM MgCl₂,
474 2.5 mM CaCl₂, 20 mM D-glucose and 0.5 mM sodium ascorbate (305 mosmol, pH 7.4, saturated
475 with 95% O₂/5% CO₂, perfused at 3 ml/min) at 30–32°C. For whole-cell recordings, we used a
476 K⁺-based pipette solution containing 142 mM K⁺-gluconate, 10 mM HEPES, 1 mM EGTA, 2.5
477 mM MgCl₂, 4 mM ATP-Mg, 0.3 mM GTP-Na, 10 mM Na₂-phosphocreatine (295 mosmol, pH
478 7.35) or a Cs⁺-based pipette solution containing 121 mM Cs⁺-methanesulfonate, 1.5 mM MgCl₂,
479 10 mM HEPES, 10 mM EGTA, 4 mM Mg-ATP, 0.3 mM Na-GTP, 10 mM Na₂-Phosphocreatine,
480 and 2 mM QX314-Cl (295 mosmol, pH 7.35). Membrane potentials were not corrected for liquid
481 junction potential (experimentally measured as 12.5 mV for the K⁺-based pipette solution and
482 9.5 mV for the Cs⁺-based pipette solution).

483

484 Neurons were visualized with video-assisted infrared differential interference contrast imaging
485 and fluorescent neurons were identified by epifluorescence imaging under a water immersion
486 objective (40×, 0.8 numerical aperture) on an upright SliceScope Pro 1000 microscope
487 (Scientifica) with an infrared IR-1000 CCD camera (DAGE-MTI). Data were low-pass filtered at
488 4 kHz and acquired at 10 kHz with an Axon Multiclamp 700B amplifier and an Axon Digidata
489 1550 Data Acquisition System under the control of Clampex 10.7 (Molecular Devices). Data
490 were analyzed offline using AxoGraph X (AxoGraph Scientific). For the photostimulation of
491 GtACR2-, iC⁺⁺-, iChloC-, or Chr2-expressing neurons, blue light was emitted from a
492 collimated light-emitting diode (LED) of 455 nm, whereas for the photostimulation of GtACR1-
493 or ReaChR-expressing neurons, red light was emitted from a LED of 617 nm. The LEDs were
494 driven by a LED driver (Mightex) under the control of an Axon Digidata 1550 Data Acquisition
495 System and Clampex 10.7. Light was delivered through the reflected light fluorescence
496 illuminator port and the 40× objective.

497

498 Synaptic currents and photocurrents were recorded in the whole-cell voltage clamp mode with
499 the Cs⁺-based patch pipette solution. Only recordings with series resistance below 20 MΩ were
500 included. EPSCs and IPSCs were recorded at the reversal potential for IPSCs (-60 mV) and
501 EPSCs (+10 mV), respectively, unless stated otherwise. Photocurrents were recorded at +10 mV
502 unless stated otherwise. For light pulse stimulation, pulse duration (0.5–10 ms) and intensity
503 (2.5–23.6 mW/mm²) were adjusted for each recording to evoke small (to minimize voltage-
504 clamp errors) but reliable monosynaptic EPSCs or IPSCs. Disynaptic IPSCs were evoked using
505 the same light pulses that were used for evoking the corresponding monosynaptic EPSCs. Light
506 pulses were delivered at 30-s interstimulus intervals. Antidromic spikes in GtACR2⁺ neurons

507 were recorded with the K⁺-based patch pipette solution in whole-cell current clamp mode or
508 with ACSF as the patch pipette solution in the loose-patch current clamp mode.

509

510 For pharmacology experiments, the baseline synaptic currents were recorded for at least 3
511 minutes in the absence of any drug. The drugs were then added to the ACSF at the following
512 concentrations: TTX (1 μM), NBQX (10 μM), (*RS*)-CPP (10 μM), SR95531 (Gabazine, 10 μM),
513 ZD7288 (20 μM), bumetanide (50 or 100 μM), TEA (1.5 mM), and 4-AP (1.5 mM). The
514 synaptic currents were recorded for at least 3 minutes in the presence of drugs. For ZD7288,
515 which did not inhibit GtACR2-induced neurotransmitter release, the efficacy of the drug was
516 monitored by examining the I_h current of cortical layer 5 pyramidal neurons.

517

518 **Fluorescent microscopy**

519 Fluorescent images were taken from live brain slices, except for the conditional expression of
520 GtACR2 in adults, where images were taken from fixed brain slices. Live brain slices were
521 prepared as described for slice electrophysiology. For the fixed brain slices, mice were
522 anesthetized by an intraperitoneal injection of a ketamine and xylazine mix (80 mg/kg and 16
523 mg/kg, respectively) and transcardially perfused with phosphate buffered saline (PBS, pH 7.4)
524 followed by 4% paraformaldehyde in PBS (pH 7.4). Brains were further fixed overnight in 4%
525 paraformaldehyde, cryoprotected with 30% sucrose in PBS, and frozen in optimum cutting-
526 temperature medium until sectioning. A HM 450 Sliding Microtome (Thermo Scientific) was
527 used to section the brains to obtain 30–50-μm coronal slices. Images were acquired on an Axio
528 Zoom.V16 Fluorescence Stereo Zoom Microscope (Zeiss) and processed using National
529 Institutes of Health ImageJ.

530

531 To determine the EYFP (or EGFP) fluorescence ratio between layer 5 and layer 2/3, one or two
532 350 μm -wide rectangular regions that were perpendicular to the pia and spanned all 6 cortical
533 layers were selected in the most transfected regions of each slice. The mean EYFP (or EGFP)
534 fluorescence was measured for layer 5 and layer 2/3 within the selected area. The mean
535 tdTomato fluorescence was measured similarly for layer 5 and layer 2/3. The mean background
536 fluorescence was measured from a nearby rectangular region (140.5 μm by 90.8 μm) where no
537 cellular EYFP (or EGFP) and tdTomato fluorescence was present. The normalized EYFP (or
538 EGFP) fluorescence ratio between layer 5 and layer 2/3 was calculated by

$$539 \frac{\text{Layer 5}_{EYFP-Background_{EYFP}}}{\text{Layer 2/3}_{EYFP-Background_{EYFP}}} / \frac{\text{Layer 5}_{tdTomato-Background_{tdTomato}}}{\text{Layer 2/3}_{tdTomato-Background_{tdTomato}}}$$

540

541 To determine the ratio of EYFP fluorescence to tdTomato fluorescence in the callosal
542 projections, one or two rectangular regions that contained the tdTomato-labeled axons were
543 selected in each slice to measure the mean EYFP and tdTomato fluorescence. The mean
544 background fluorescence was measured in a nearby cortical area spanning the same layers. The
545 ratio of EYFP fluorescence to tdTomato fluorescence was calculated by

$$546 \frac{\text{Fluorescence}_{EYFP-Background_{EYFP}}}{\text{Fluorescence}_{tdTomato-Background_{tdTomato}}}$$

547

548 **Statistics**

549 All reported sample numbers (n) represent biological replicates that are the numbers of recorded
550 neurons for electrophysiology or the numbers of analyzed regions of interest (ROI) for
551 fluorescent images. Statistical analyses were performed with Prism 7 (GraphPad Software). We
552 first determined whether the data were normally distributed by performing the D'Agostino &

553 Pearson test, Shapiro-Wilk test, and KS test. If all data within one experiment passed all three
554 normality tests, we then performed the statistical test that assumes a Gaussian distribution.
555 Otherwise, we performed the statistical test that assumed a non-Gaussian distribution. All
556 statistical tests were two-tailed with an alpha of 0.05.

557

558 Wilcoxon matched-pairs signed rank test was used for Figure 1F,K; Figure 2B,D,F,J; Figure 2-
559 supplement 2B,E; Figure 2-supplement 3B (EPSCs); Figure 3B; and Figure 3-supplement 1C.

560 Paired *t* test was used for Figure 1G,J; Figure 2H; Figure 2-supplement 1D; and Figure 2-
561 supplement 3B (photocurrents),D. *t* test with Welch's correction was used for Figure 4E and

562 Figure 5C (WT vs. Kv2.1C). Mann-Whitney test was used for Figure 5C (WT vs. Kv2.1C-

563 linker-T1cnC),F,G,H,J. One-way ANOVA with Greenhouse-Geisser correction and Tukey

564 multiple comparisons was used for Figure 3D,F. Kruskal-Wallis test with Dunn's multiple

565 comparisons was used for Figure 4B.

566

567 **Acknowledgments**

568 We thank Elena Govorunova and John Spudich for discussions and the pLenti-UbiC-GtACR2-

569 EYFP and pLenti-UbiC-GtACR1-EYFP plasmids, Anirvan Ghosh for the pCAG-tdTomato

570 plasmid, Karl Deisseroth for the pAAV-CaMKII α -iC $^{++}$ -TS-EYFP and pAAV-EF1 α -DIO-iC $^{++}$ -

571 TS-EYFP plasmids, Matthew Caudill and Massimo Scanziani for the pAAV-EF1 α -DIO-iChloC-

572 T2A-mCherry plasmid, Zhuo-Hua Pan for the pAAV-EF1 α -DIO-hChR2(H134R)-EYFP-

573 Kv2.1C plasmid, Edward Boyden for the pAAV-hSyn-soCoChR-EGFP plasmid, and Hsiao-

574 Tuan Chao and Matthew Caudill for comments on an earlier version of the manuscript. This

575 work was supported in part by a Whitehall Foundation Research Grant (#2015-05-54, to M.X.).

576 J.E.M is part of the Baylor College of Medicine Medical Scientist Training Program and a
577 McNair M.D./Ph.D. Student Scholar supported by the McNair Medical Institute at the Robert
578 and Janice McNair Foundation. M.X. is a Caroline DeLuca Scholar.

579

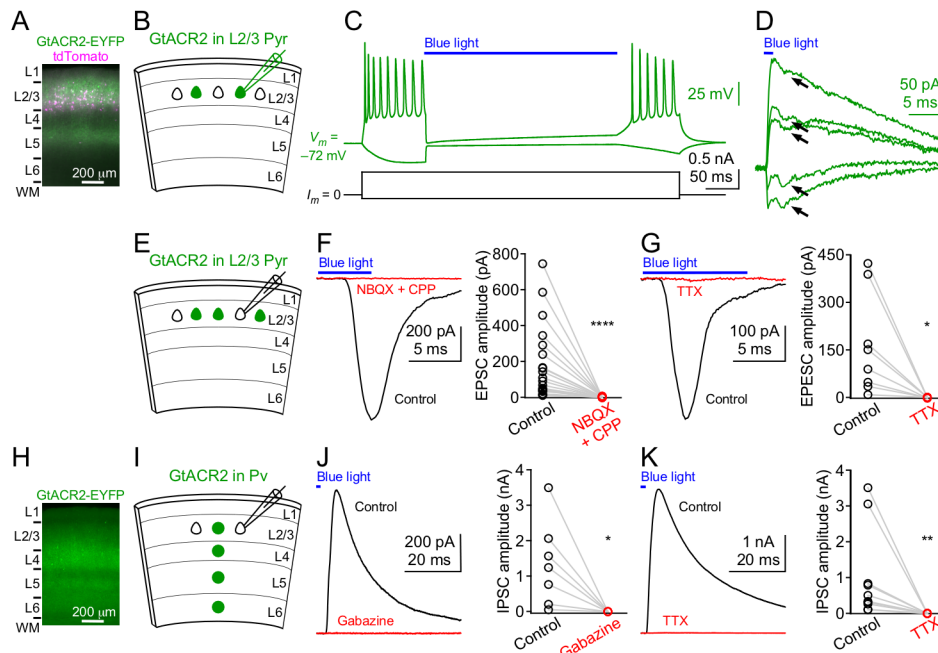
580 **Competing interests**

581 The authors declare no competing financial interests.

582

583 **Figures and legends**

Figure 1



584 **Figure 1. Light activation of GtACR2 causes excitatory and inhibitory neurons to release**
 585 **neurotransmitter.**

586 (A) A representative fluorescent image of the visual cortex showing GtACR2-EYFP and
 587 tdTomato expression in a subset of layer 2/3 pyramidal neurons. Note the strong EYFP
 588 fluorescence in layer 5 that contains the axons of layer 2/3 pyramidal neurons. L, layer; WM,
 589 white matter.

590 (B) Schematic of slice experiments in (C,D). GtACR2 in a subset of layer 2/3 pyramidal neurons.

591 (C) Membrane potentials (upper panel) in response to somatic current injections (lower panel)
 592 from a GtACR2⁺ neuron. Blue light activation of GtACR2 suppressed the action potentials
 593 evoked by current injections ($n = 5$).

594 **(D)** Blue light-induced membrane currents recorded at membrane potentials of -75, -77, -78, -79,
595 and -80 mV from the same GtACR2⁺ neuron in (C). Note the EPSC-like inward currents
596 (arrows) superimposed on the GtACR2-mediated photocurrents ($n = 2$).

597 **(E)** Schematic of slice experiments in (F,G). GtACR2 in a subset of layer 2/3 pyramidal neurons.

598 **(F)** Left, photoactivation of GtACR2 generated EPSCs in a GtACR2⁻ neuron, which were
599 abolished by the glutamate receptor antagonists, NBQX and CPP. Right, summary graph of
600 similar experiments ($n = 17, P < 0.0001$).

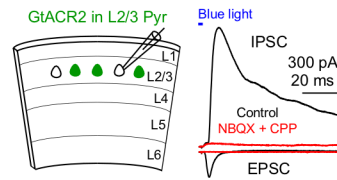
601 **(G)** Left, photoactivation of GtACR2 generated EPSCs in a GtACR2⁻ neuron, which were
602 abolished by the voltage-gated sodium channel blocker, TTX. Right, summary graph of similar
603 experiments ($n = 8, P = 0.02$).

604 **(H)** A representative fluorescent image of the visual cortex showing GtACR2-EYFP expression
605 in Pv neurons.

606 **(I,J,K)** As in (E,F,G), but for GtACR2 in Pv neurons. GtACR2 activation-induced IPSCs were
607 abolished by the GABA_A receptor antagonist, Gabazine (J, $n = 7, P = 0.02$) or TTX (K, $n = 10, P$
608 $= 0.002$).

609

Figure 1-supplement 1



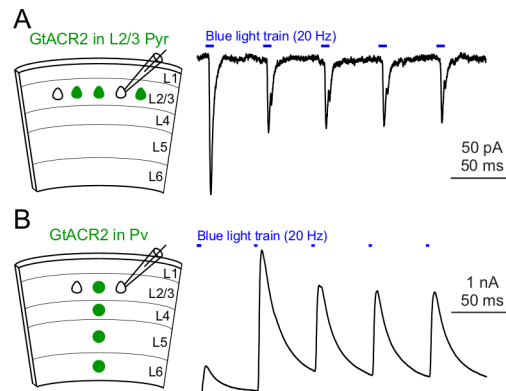
610

611 **Figure 1-supplement 1. Recruitment of inhibitory neurons by activating GtACR2 in**
612 **excitatory neurons.**

613 Left, schematic of slice experiments. GtACR2 in a subset of layer 2/3 pyramidal neurons. Right,
614 photoactivation of GtACR2 generated an EPSC (inward current) and IPSC (outward current) in a
615 GtACR2⁻ neuron. The IPSC was abolished by the glutamatergic receptor antagonists, NBQX and
616 CPP (red trace), indicating its disynaptic nature ($n = 3$).

617

Figure 1-supplement 2



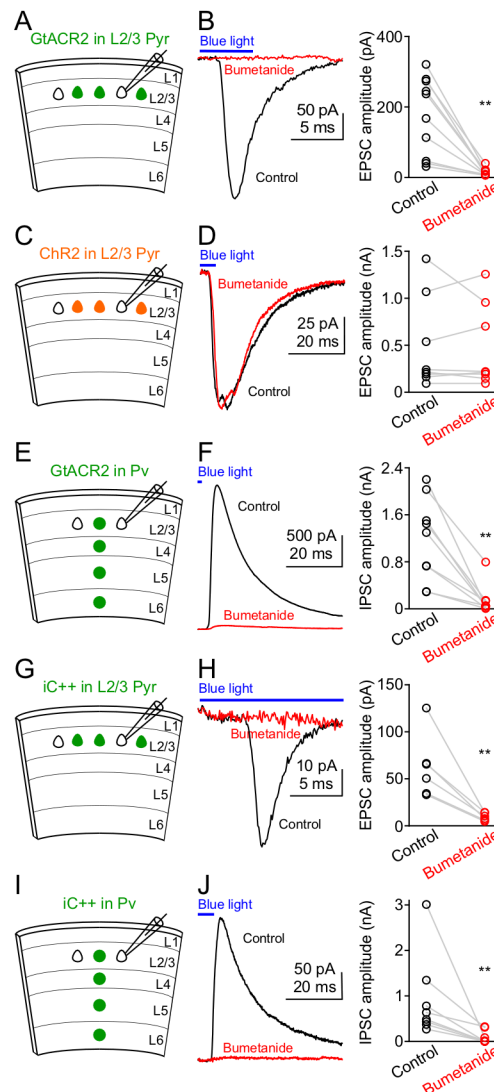
618

619 **Figure 1-supplement 2. Repetitive activation of GtACR2 reliably causes neurotransmitter**
620 **release.**

621 (A) Left, schematic of slice experiments. GtACR2 in a subset of layer 2/3 pyramidal neurons.
622 Right, a 20-Hz train of blue-light pulses activated GtACR2 to generate EPSCs in a GtACR2⁻
623 neuron ($n = 11$).

624 (B) As in (A), but for GtACR2 in Pv neurons. A 20-Hz train of blue-light pulses activated
625 GtACR2 to generate IPSCs in a GtACR2⁻ neuron ($n = 14$).

Figure 2



626

627 **Figure 2. Reducing intracellular chloride concentrations diminishes the neurotransmitter**
628 **release induced by activation GtACR2 or iC++.**

629 (A) Schematic of slice experiments in (B). GtACR2 in a subset of layer 2/3 pyramidal neurons.

630 (B) Left, photoactivation of GtACR2 generated EPSCs in a GtACR2⁻ neuron, which were

631 diminished by decreasing intracellular chloride concentrations with an NKCC1 blocker,

632 bumetanide. Right, summary graph of similar experiments ($n = 10$, $P = 0.002$).

633 (C,D) As in (A,B), but for Chr2. Chr2 activation-induced EPSCs were not affected by
634 bumetanide ($n = 8$, $P = 0.9$).

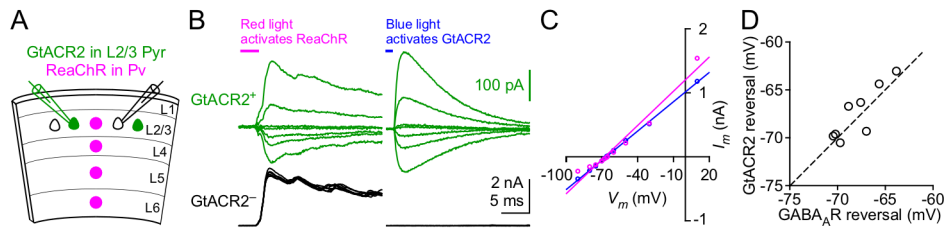
635 (E,F) As in (A,B), but for GtACR2 in Pv neurons. GtACR2 activation-induced IPSCs were
636 diminished by bumetanide ($n = 9$, $P = 0.004$).

637 (G,H) As in (A,B), but for iC⁺⁺. iC⁺⁺-induced EPSCs were diminished by bumetanide ($n = 6$, P
638 = 0.009).

639 (I,J) As in (E,F), but for iC⁺⁺. iC⁺⁺-induced IPSCs were diminished by bumetanide ($n = 8$, $P =$
640 0.008).

641

Figure 2-supplement 1



642

643 **Figure 2-supplement 1. The reversal potential of GtACR2 at the soma is similar to that of**
644 **GABA_A receptor.**

645 (A) Schematic of slice experiments in (B). GtACR2 in a subset of layer 2/3 pyramidal neurons
646 and ReaChR in Pv neurons.

647 (B) In a GtACR2⁺ neuron, GABAergic IPSCs induced by activating ReaChR in Pv neurons (left
648 panel) and GtACR2-mediated photocurrents (right panel) were sequentially recorded at different
649 membrane potentials. The example traces show the currents at -50, -60, -65, -66, -68, -70, and -
650 75 mV. A GtACR2⁻ neuron was simultaneously recorded at the membrane potential of +10 mV
651 to ensure that the blue light did not generate IPSCs (right panel).

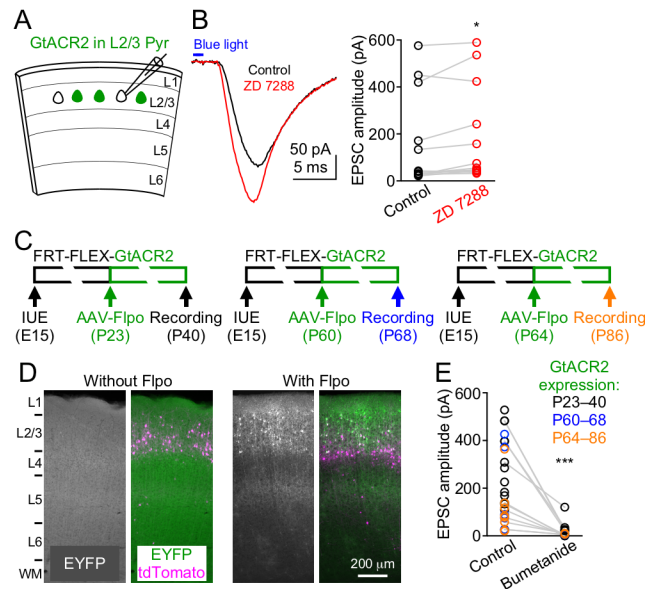
652 (C) The amplitudes of IPSCs and GtACR2 photocurrents were plotted as a function of the
653 membrane potentials for the GtACR2⁺ neuron in (B). Each set of data were fit with linear
654 regression and the reversal potentials were determined by the V_m -axis intercepts.

655 (D) Summary graph of similar experiments in (B,C) where the reversal potential of IPSCs was
656 plotted against that of GtACR2 photocurrents for each GtACR2⁺ neuron. All data points fall
657 close to the dotted unity line and there is no significant difference between the reversal potentials
658 of IPSCs and photocurrents ($n = 8$, $P = 0.4$).

659

660

Figure 2-supplement 2



661

662 **Figure 2-supplement 2. GtACR2-induced neurotransmitter release is not due to rebound**
663 **depolarization or its long-term expression throughout development.**

664 (A) Schematic of slice experiments in (B). GtACR2 in a subset of layer 2/3 pyramidal neurons.

665 (B) Left, photoactivation of GtACR2 generated EPSCs in a GtACR2⁻ neuron, which were not

666 decreased by blocking the I_h current with ZD7288 (20 μM). Right, summary graph of similar

667 experiments showing that the EPSC amplitudes were slightly increased by ZD7288 (*n* = 12, *P* =

668 0.03).

669 (C) Schematics of conditional expression of GtACR2 in a subset of layer 2/3 pyramidal neurons.

670 A Flpo-dependent plasmid (FRT-FLEX-GtACR2) was electroporated at embryonic day 15 (E15)

671 and AAV9-hSyn-Flpo was injected into the electroporated mice at different postnatal days (P23,

672 P60, or P64). Green bars indicate the approximate GtACR2 expression time windows.

673 (D) Left, representative fluorescent images of the visual cortex obtained at postnatal day 73

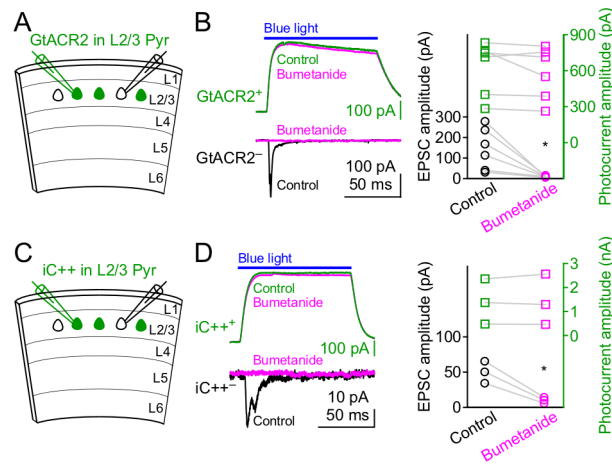
674 showing that without injection of AAV9-hSyn-Flpo, transfected neurons (labeled by tdTomato)

675 did not express GtACR2-EYFP (left panel, $n = 5$ mice). Note that the image from the EYFP
676 channel was overexposed to show no EYFP⁺ neurons. Right, representative fluorescent images
677 of the visual cortex obtained at postnatal day 40 showing that the expression of GtACR2-EYFP
678 in transfected neurons was turned on by the injection of AAV9-hSyn-Flpo at postnatal day 23
679 (right panel, $n = 7$ mice).

680 (E) Photoactivation of GtACR2 generated EPSCs in GtACR2⁻ neurons when GtACR2 was
681 expressed during 3 different time windows as indicated in (C). Bumetanide was applied in a
682 subset of experiments and the EPSCs were diminished ($n = 12$, $P = 0.0005$).

683

Figure 2-supplement 3



684

685 **Figure 2-supplement 3. Bumetanide does not affect GtACR2 and iC⁺⁺-mediated**
686 **photocurrents.**

687 (A) Schematic of slice experiments in (B). GtACR2 in a subset of layer 2/3 pyramidal neurons.

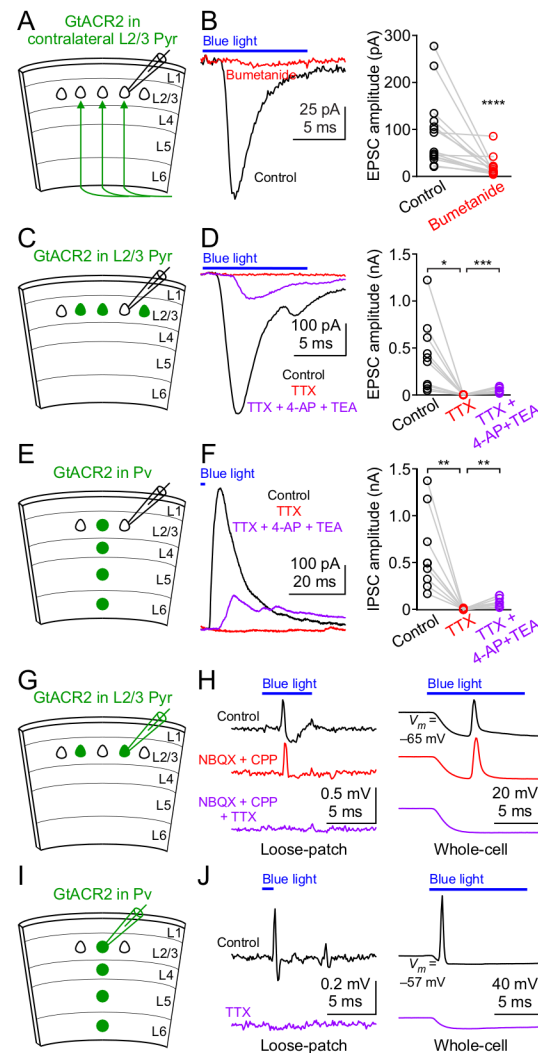
688 (B) Left, photoactivation of GtACR2 generated photocurrents in a GtACR2⁺ neuron (top panel,
689 recorded at the membrane potential of +10 mV) and EPSCs in a simultaneously recorded
690 GtACR2⁻ neuron (bottom panel, recorded at the membrane potential of -60 mV). Bumetanide
691 diminished the EPSCs (circle symbols) without affecting the photocurrents (square symbols).

692 Right, summary graph of similar experiments ($n = 6$; EPSCs, $P = 0.03$; photocurrents, $P = 0.3$).

693 (C,D) As in (A,B), but for iC⁺⁺. Bumetanide diminished the EPSCs without affecting the

694 photocurrents ($n = 3$; EPSCs, $P = 0.03$; photocurrents, $P = 0.7$).

Figure 3



695

696 **Figure 3. GtACR2 activation directly depolarizes the distal axon and presynaptic terminals**
 697 **and can result in antidromic spikes.**

698 (A) Schematic of slice experiments in (B). GtACR2 in a subset of layer 2/3 pyramidal neurons in
 699 the contralateral hemisphere.

700 (B) Left, photoactivation of GtACR2 in the callosal axons, severed from their somas, generated
 701 EPSCs in a GtACR2⁻ neuron, which were diminished by bumetanide. Right, summary graph of
 702 similar experiments ($n = 15$, $P < 0.0001$).

703 (C) Schematic of slice experiments in (D). GtACR2 in a subset of layer 2/3 pyramidal neurons.

704 (D) Left, photoactivation of GtACR2 generated EPSCs in a GtACR2⁻ neuron, which were
705 abolished by TTX, but partially recovered by the addition of voltage-gated potassium channel
706 blockers, 4-AP (1.5 mM) and TEA (1.5 mM). Right, summary graph of similar experiments ($n =$
707 10; TTX vs. control, $P = 0.02$, average EPSC amplitude in TTX was 2% of control; TTX + 4-AP
708 + TEA vs. TTX, $P = 0.0004$, average EPSC amplitude in TTX + 4-AP + TEA was 35% of
709 control).

710 (E,F) As in (C,D), but for Pv neurons. GtACR2 activation-induced IPSCs were abolished by
711 TTX, but partially recovered by 4-AP and TEA ($n = 9$; TTX vs. control, $P = 0.006$, average IPSC
712 amplitude in TTX was 0.9% of control; TTX + 4-AP + TEA vs. TTX, $P = 0.008$, average IPSC
713 amplitude in TTX + 4-AP + TEA was 23% of control).

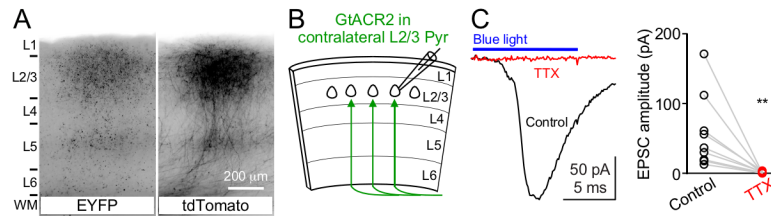
714 (G) Schematic of slice experiments in (H). GtACR2 in a subset of layer 2/3 pyramidal neurons.

715 (H) Photoactivation of GtACR2 generated antidromic spikes in GtACR2⁺ pyramidal neurons,
716 which were not affected by NBQX and CPP, but were abolished by TTX in both loose-patch
717 (left panel) and whole-cell (right panel) recordings. In the whole-cell recordings, the resting
718 membrane potentials of those neurons that generated antidromic spikes are -68.1 ± 1.7 mV
719 (mean \pm s.e.m., $n = 21$).

720 (I,J) As in (G,H), but for Pv neurons. The antidromic spikes in GtACR2⁺ Pv neurons were
721 abolished by TTX. In the whole-cell recordings, the resting membrane potentials of those
722 neurons that generated antidromic spikes are -60.0 ± 2.4 mV (mean \pm s.e.m., $n = 7$).

723

Figure 3-supplement 1



724

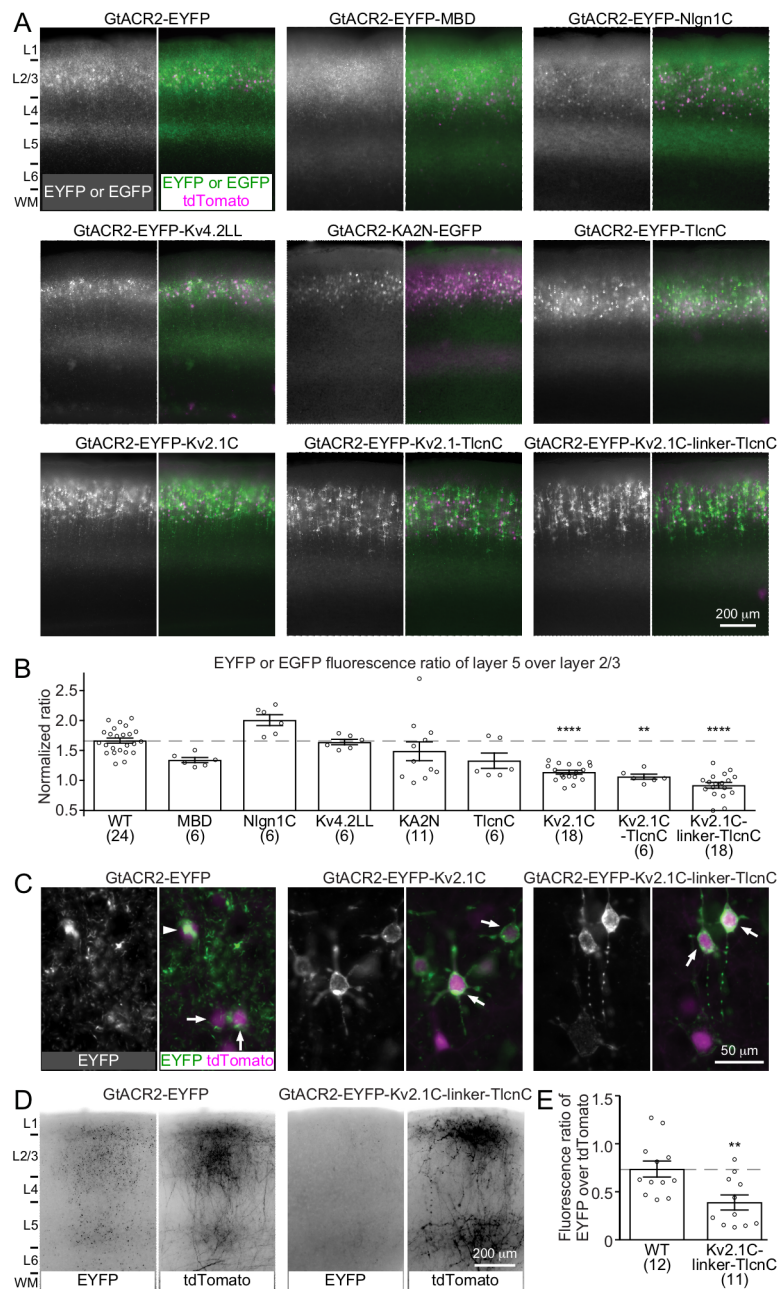
725 **Figure 3-supplement 1. Activation of GtACR2 in the callosal axons causes**
726 **neurotransmitter release.**

727 (A) GtACR2-EYFP and tdTomato were expressed in a subset of layer 2/3 pyramidal neurons in
728 the visual cortex of one hemisphere. Representative fluorescent images of the contralateral
729 hemisphere showing GtACR2-EYFP (left panel) in the callosal projections labeled by tdTomato
730 (right panel). L, layer; WM, white matter.

731 (B) Schematic of slice experiments in (C). GtACR2-EYFP in a subset of layer 2/3 pyramidal
732 neurons in the contralateral hemisphere.

733 (C) Left, photoactivation of GtACR2 in the callosal axons generated EPSCs in a GtACR2⁻
734 neuron, which were abolished by TTX. Right, summary graph of similar experiments ($n = 9$, $P =$
735 0.004).

Figure 4



736

737 **Figure 4. Targeting GtACR2 to neuronal somatodendritic domain.**

738 (A) Wild type (WT) GtACR2 and its variants tagged with EYFP or EGFP were expressed along
 739 with tdTomato in a subset of layer 2/3 pyramidal neurons. Representative fluorescent images of
 740 the cortices showing the distribution of GtACR2. Note the strong EYFP fluorescence in layer 5

741 for WT GtACR2 and weak EYFP fluorescence for some somatodendritically targeted GtACR2
742 variants (e.g., Kv2.1C-linker-TlcnC).

743 **(B)** The EYFP or EGFP fluorescence ratio between layer 5 and layer 2/3 was normalized by the
744 tdTomato fluorescence ratio between layer 5 and layer 2/3. A reduction in the normalized EYFP
745 or EGFP fluorescence ratio indicates a shift of the EYFP or EGFP distribution from the axon to
746 somatodendritic domain.

747 **(C)** Representative fluorescent images of electroporated neurons showing that GtACR2-EYFP-
748 Kv2.1C and GtACR2-EYFP-Kv2.1C-linker-TlcnC were more concentrated on the membranes at
749 the soma and proximal dendrites (arrows) than GtACR2-EYFP. Note the intracellular
750 aggregation of GtACR2-EYFP (arrow head).

751 **(D)** Representative fluorescent images of the contralateral hemisphere showing less GtACR2-
752 EYFP-Kv2.1C-linker-TlcnC in the callosal projections than GtACR2-EYFP. The callosal
753 projections were labeled by tdTomato.

754 **(E)** The ratio of EYFP fluorescence to tdTomato fluorescence in the callosal projections in the
755 contralateral hemisphere.

756 The numbers of analyzed slices were indicated in the panel. The columns and error bars are
757 mean \pm s.e.m. ** $P < 0.01$, **** $P < 0.0001$.

758

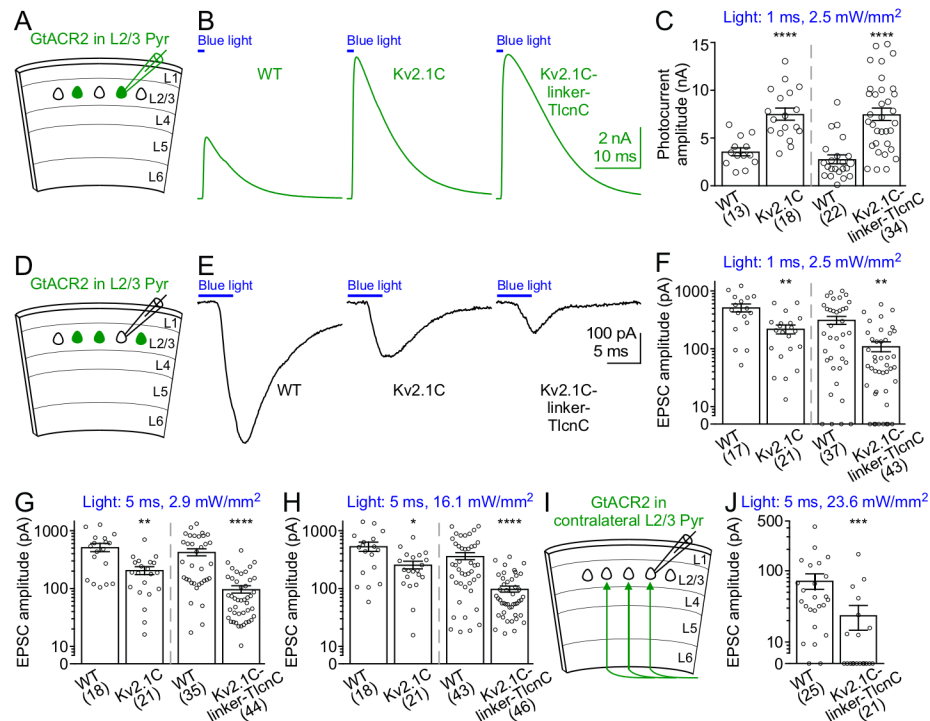
759 **Figure 4-supplement 1. Sequences of somatodendritic targeting motifs.**

760 Black, amino acid sequences of somatodendritic targeting motifs; blue, GtACR2; green, EYFP

761 or EGFP; magenta, linker.

Motif	Sequence
MBD	<i>GtACR2-EYFP-GSGSGTRGSGS-</i> RDQPLNSKKKKRLLSFRDVFEEEDSD
Nlgn1C	<i>GtACR2-EYFP-VVLRTACPPDYTLAMRRSPDDIPLMTPNTITM</i>
Kv4.2LL	<i>GtACR2-EYFP-FETQHHLHLCLEKTT</i>
KA2N	<i>GtACR2-GSGGGTGGSGGT-</i> MPAELLLLIVAFANPSCQVLSLRMAAILDDQTVCGRGERLA LALAREQINGIIEVPAKARVEVDIFELQRDSQYETTDTCMCQILP KGVVSVLGPSSSPASASTVSHICGEKEIPHIKVGPEETPRLQYLR FASVSLYPSNEDVSLAVS- <i>GASGGT-EGFP</i>
TlcnC	<i>GtACR2-EYFP-AESPADGEVFAIQLTSS</i>
Kv2.1C	<i>GtACR2-EYFP-</i> QSQPILNTKEMAPQSKPPEELEMSSMPSPVAPLPARTEGVIDMR SMSSIDSFISCATDFPEATRF
Kv2.1C-TlcnC	<i>GtACR2-EYFP-</i> QSQPILNTKEMAPQSKPPEELEMSSMPSPVAPLPARTEGVIDMR SMSSIDSFISCATDFPEATRF-AESPADGEVFAIQLTSS
Kv2.1C-linker-TlcnC	<i>GtACR2-EYFP-</i> QSQPILNTKEMAPQSKPPEELEMSSMPSPVAPLPARTEGVIDMR SMSSIDSFISCATDFPEATRF- <i>GSGSGSGSGS-</i> AESPADGEVFAIQLTSS

Figure 5



762

763 **Figure 5. Activation of somatodendritically targeted GtACR2 variants generate larger**
 764 **photocurrents but cause less neurotransmitter release than wild type GtACR2.**

765 (A) Schematic of slice experiments in (B,C). GtACR2-EYFP, GtACR2-EYFP-Kv2.1C, or
 766 GtACR2-EYFP-Kv2.1C-linker-TlcnC in a subset of layer 2/3 pyramidal neurons.

767 (B) Somatic photocurrents recorded at the membrane potential of +10 mV from GtACR2-
 768 EYFP-, GtACR2-EYFP-Kv2.1C-, or GtACR2-EYFP-Kv2.1C-linker-TlcnC-expressing neurons
 769 in response to a blue light pulse of 1-ms and 2.5-mW/mm².

770 (C) Summary graph showing the photocurrent peak amplitudes of GtACR2-EYFP-Kv2.1C and
 771 GtACR2-EYFP-Kv2.1C-linker-TlcnC were larger than those of GtACR2-EYFP.

772 (D,E) As in (A,B), but for recording EPSCs in GtACR2⁻ layer 2/3 pyramidal neurons in response
 773 to a blue light pulse of 5-ms and 2.9-mW/mm².

774 (F,G,H) Summary graphs showing the EPSC amplitudes in response to a blue light pulse of 1-
775 ms and 2.5 mW/mm² (F), 5-ms and 2.9 mW/mm² (G), or 5-ms and 16.1 mW/mm² (H).
776 (I) Schematic of slice experiments in (J). GtACR2-EYFP or GtACR2-EYFP-Kv2.1C-linker-
777 TlcnC in a subset of layer 2/3 pyramidal neurons in the contralateral hemisphere.
778 (J) Summary graphs showing the EPSC amplitudes in response to a blue light pulse of 5-ms and
779 23.6 mW/mm².
780 The numbers of recorded neurons were indicated in the panel. The columns and error bars are
781 mean ± s.e.m. * $P < 0.05$, ** $P < 0.01$, *** $P < 0.001$, **** $P < 0.0001$.

782

783 References

- 784 Allen, B.D., Singer, A.C., Boyden, E.S., 2015. Principles of designing interpretable optogenetic
785 behavior experiments. *Learn. Mem.* 22, 232–238. doi:10.1101/lm.038026.114
- 786 Baker, C.A., Elyada, Y.M., Parra, A., Bolton, M.M., 2016. Cellular resolution circuit mapping
787 with temporal-focused excitation of soma-targeted channelrhodopsin. *Elife* 5, 11981.
788 doi:10.7554/eLife.14193
- 789 Ben-Ari, Y., 2017. NKCC1 Chloride Importer Antagonists Attenuate Many Neurological and
790 Psychiatric Disorders. *Trends Neurosci* 40, 536–554. doi:10.1016/j.tins.2017.07.001
- 791 Ben-Ari, Y., 2002. Excitatory actions of gaba during development: the nature of the nurture. *Nat*
792 *Rev Neurosci* 3, 728–739. doi:10.1038/nrn920
- 793 Berndt, A., Lee, S.Y., Ramakrishnan, C., Deisseroth, K., 2014. Structure-guided transformation
794 of channelrhodopsin into a light-activated chloride channel. *Science* 344, 420–424.
795 doi:10.1126/science.1252367
- 796 Berndt, A., Lee, S.Y., Wietek, J., Ramakrishnan, C., Steinberg, E.E., Rashid, A.J., Kim, H., Park,
797 S., Santoro, A., Frankland, P.W., Iyer, S.M., Pak, S., Åhrlund-Richter, S., Delp, S.L.,
798 Malenka, R.C., Josselyn, S.A., Carlén, M., Hegemann, P., Deisseroth, K., 2015. Structural
799 foundations of optogenetics: Determinants of channelrhodopsin ion selectivity. *Proc Natl*
800 *Acad Sci USA*. doi:10.1073/pnas.1523341113
- 801 Boyden, E.S., Zhang, F., Bamberg, E., Nagel, G., Deisseroth, K., 2005. Millisecond-timescale,
802 genetically targeted optical control of neural activity. *Nat Neurosci* 8, 1263–1268.
803 doi:10.1038/nn1525
- 804 Chow, B.Y., Han, X., Dobry, A.S., Qian, X., Chuong, A.S., Li, M., Henninger, M.A., Belfort,
805 G.M., Lin, Y., Monahan, P.E., Boyden, E.S., 2010. High-performance genetically targetable
806 optical neural silencing by light-driven proton pumps. *Nature* 463, 98–102.
807 doi:10.1038/nature08652
- 808 Chuong, A.S., Miri, M.L., Busskamp, V., Matthews, G.A.C., Acker, L.C., Sørensen, A.T.,
809 Young, A., Klapoetke, N.C., Henninger, M.A., Kodandaramaiah, S.B., Ogawa, M.,

- 810 Ramanlal, S.B., Bandler, R.C., Allen, B.D., Forest, C.R., Chow, B.Y., Han, X., Lin, Y., Tye,
811 K.M., Roska, B., Cardin, J.A., Boyden, E.S., 2014. Noninvasive optical inhibition with a
812 red-shifted microbial rhodopsin. *Nature neuroscience*. doi:10.1038/nn.3752
- 813 Forli, A., Vecchia, D., Binini, N., Succol, F., Bovetti, S., Moretti, C., Nespoli, F., Mahn, M.,
814 Baker, C.A., Bolton, M.M., Yizhar, O., Fellin, T., 2018. Two-Photon Bidirectional Control
815 and Imaging of Neuronal Excitability with High Spatial Resolution In Vivo. *Cell Rep* 22,
816 3087–3098. doi:10.1016/j.celrep.2018.02.063
- 817 Govorunova, E.G., Sineshchekov, O.A., Janz, R., Liu, X., Spudich, J.L., 2015. Natural light-
818 gated anion channels: A family of microbial rhodopsins for advanced optogenetics. *Science*
819 349, 647–650. doi:10.1126/science.aaa7484
- 820 Govorunova, E.G., Sineshchekov, O.A., Li, H., Spudich, J.L., 2017a. Microbial Rhodopsins:
821 Diversity, Mechanisms, and Optogenetic Applications. *Annu. Rev. Biochem.* 86, 845–872.
822 doi:10.1146/annurev-biochem-101910-144233
- 823 Govorunova, E.G., Sineshchekov, O.A., Rodarte, E.M., Janz, R., Morelle, O., Melkonian, M.,
824 Wong, G.K.S., Spudich, J.L., 2017b. The Expanding Family of Natural Anion
825 Channelrhodopsins Reveals Large Variations in Kinetics, Conductance, and Spectral
826 Sensitivity. *Sci Rep* 7, 43358. doi:10.1038/srep43358
- 827 Han, X., Boyden, E.S., 2007. Multiple-color optical activation, silencing, and desynchronization
828 of neural activity, with single-spike temporal resolution. *PLoS ONE* 2, e299.
829 doi:10.1371/journal.pone.0000299
- 830 Han, X., Chow, B.Y., Zhou, H., Klapoetke, N.C., Chuong, A., Rajimehr, R., Yang, A., Baratta,
831 M.V., Winkle, J., Desimone, R., Boyden, E.S., 2011. A high-light sensitivity optical neural
832 silencer: development and application to optogenetic control of non-human primate cortex.
833 *Front. Syst. Neurosci.* 5, 18. doi:10.3389/fnsys.2011.00018
- 834 Jang, I.S., Nakamura, M., Ito, Y., Akaike, N., 2006. Presynaptic GABA_A receptors facilitate
835 spontaneous glutamate release from presynaptic terminals on mechanically dissociated rat
836 CA3 pyramidal neurons. *Neuroscience* 138, 25–35. doi:10.1016/j.neuroscience.2005.11.001
- 837 Khirug, S., Yamada, J., Afzalov, R., Voipio, J., Khiroug, L., Kaila, K., 2008. GABAergic
838 Depolarization of the Axon Initial Segment in Cortical Principal Neurons Is Caused by the
839 Na-K-2Cl Cotransporter NKCC1. *J Neurosci* 28, 4635–4639.
840 doi:10.1523/JNEUROSCI.0908-08.2008
- 841 Kim, C.K., Adhikari, A., Deisseroth, K., 2017. Integration of optogenetics with complementary
842 methodologies in systems neuroscience. *Nat Rev Neurosci* 18, 222–235.
843 doi:10.1038/nrn.2017.15
- 844 Lewis, T.L., Mao, T., Svoboda, K., Arnold, D.B., 2009. Myosin-dependent targeting of
845 transmembrane proteins to neuronal dendrites. *Nat Neurosci* 12, 568–576.
846 doi:10.1038/nn.2318
- 847 Li, X., Gutierrez, D.V., Hanson, M.G., Han, J., Mark, M.D., Chiel, H., Hegemann, P.,
848 Landmesser, L.T., Herlitze, S., 2005. Fast noninvasive activation and inhibition of neural
849 and network activity by vertebrate rhodopsin and green algae channelrhodopsin. *Proc Natl*
850 *Acad Sci USA* 102, 17816–17821. doi:10.1073/pnas.0509030102
- 851 Lim, S.T., Antonucci, D.E., Scannevin, R.H., Trimmer, J.S., 2000. A novel targeting signal for
852 proximal clustering of the Kv2.1 K⁺ channel in hippocampal neurons. *Neuron* 25, 385–397.
- 853 Lin, J.Y., Knutsen, P.M., Muller, A., Kleinfeld, D., Tsien, R.Y., 2013. ReaChR: a red-shifted
854 variant of channelrhodopsin enables deep transcranial optogenetic excitation. *Nat Neurosci*
855 16, 1499–1508. doi:10.1038/nn.3502

- 856 Madisen, L., Garner, A.R., Shimaoka, D., Chuong, A.S., Klapoetke, N.C., Li, L., van der Bourg,
857 A., Niino, Y., Egolf, L., Monetti, C., Gu, H., Mills, M., Cheng, A., Tasic, B., Nguyen, T.N.,
858 Sunkin, S.M., Benucci, A., Nagy, A., Miyawaki, A., Helmchen, F., Empson, R.M., Knöpfel,
859 T., Boyden, E.S., Reid, R.C., Carandini, M., Zeng, H., 2015. Transgenic mice for
860 intersectional targeting of neural sensors and effectors with high specificity and
861 performance. *Neuron* 85, 942–958. doi:10.1016/j.neuron.2015.02.022
- 862 Madisen, L., Zwingman, T.A., Sunkin, S.M., Oh, S.W., Zariwala, H.A., Gu, H., Ng, L.L.,
863 Palmiter, R.D., Hawrylycz, M.J., Jones, A.R., Lein, E.S., Zeng, H., 2010. A robust and high-
864 throughput Cre reporting and characterization system for the whole mouse brain. *Nat*
865 *Neurosci* 13, 133–140. doi:10.1038/nn.2467
- 866 Mahn, M., Prigge, M., Ron, S., Levy, R., Yizhar, O., 2016. Biophysical constraints of
867 optogenetic inhibition at presynaptic terminals. *Nat Neurosci* 19, 554–556.
868 doi:10.1038/nn.4266
- 869 Mahn, M., Gibor, L., Malina, K.C-K., Patil, P., Printz, Y., Oring, S., Levy, R., Lampl, I., Yizhar,
870 O., 2017. High-efficiency optogenetic silencing with soma-targeted anion-conducting
871 channelrhodopsins. *bioRxiv*. doi: <https://doi.org/10.1101/225847>
- 872 Malyshev, A.Y., Roshchin, M.V., Smirnova, G.R., Dolgikh, D.A., Balaban, P.M., Ostrovsky,
873 M.A., 2017. Chloride conducting light activated channel GtACR2 can produce both
874 cessation of firing and generation of action potentials in cortical neurons in response to light.
875 *Neurosci. Lett.* 640, 76–80. doi:10.1016/j.neulet.2017.01.026
- 876 Mardinly, A.R., Oldenburg, I.A., Pégard, N.C., Sridharan, S., Lyall, E.H., Chesnov, K.,
877 Brohawn, S.G., Waller, L., Adesnik, H., 2018. Precise multimodal optical control of neural
878 ensemble activity. *Nat Neurosci* 466, 123. doi:10.1038/s41593-018-0139-8
- 879 Marty, A., Llano, I., 2005. Excitatory effects of GABA in established brain networks. *Trends*
880 *Neurosci* 28, 284–289. doi:10.1016/j.tins.2005.04.003
- 881 Mauss, A.S., Busch, C., Borst, A., 2017. Optogenetic Neuronal Silencing in *Drosophila* during
882 Visual Processing. *Sci Rep* 7, 13823. doi:10.1038/s41598-017-14076-7
- 883 Mitsui, S., Saito, M., Hayashi, K., Mori, K., Yoshihara, Y., 2005. A novel phenylalanine-based
884 targeting signal directs telencephalin to neuronal dendrites. *Journal of Neuroscience* 25,
885 1122–1131. doi:10.1523/JNEUROSCI.3853-04.2005
- 886 Mohamed, G.A., Cheng, R.-K., Ho, J., Krishnan, S., Mohammad, F., Claridge-Chang, A.,
887 Jesuthasan, S., 2017. Optical inhibition of larval zebrafish behaviour with anion
888 channelrhodopsins. *BMC Biol* 15, 103. doi:10.1186/s12915-017-0430-2
- 889 Mohammad, F., Stewart, J.C., Ott, S., Chlebikova, K., Chua, J.Y., Koh, T.-W., Ho, J., Claridge-
890 Chang, A., 2017. Optogenetic inhibition of behavior with anion channelrhodopsins. *Nat*
891 *Methods* 14, 271–274. doi:10.1038/nmeth.4148
- 892 Nagel, G., Szellas, T., Huhn, W., Kateriya, S., Adeishvili, N., Berthold, P., Ollig, D., Hegemann,
893 P., Bamberg, E., 2003. Channelrhodopsin-2, a directly light-gated cation-selective membrane
894 channel. *Proc Natl Acad Sci USA* 100, 13940–13945. doi:10.1073/pnas.1936192100
- 895 Owens, D.F., Boyce, L.H., Davis, M.B., Kriegstein, A.R., 1996. Excitatory GABA responses in
896 embryonic and neonatal cortical slices demonstrated by gramicidin perforated-patch
897 recordings and calcium imaging. *J Neurosci* 16, 6414–6423.
- 898 Petreanu, L., Mao, T., Sternson, S.M., Svoboda, K., 2009. The subcellular organization of
899 neocortical excitatory connections. *Nature* 457, 1142–1145. doi:10.1038/nature07709
- 900 Price, G.D., Trussell, L.O., 2006. Estimate of the chloride concentration in a central
901 glutamatergic terminal: a gramicidin perforated-patch study on the calyx of Held. *Journal of*

- 902 Neuroscience 26, 11432–11436. doi:10.1523/JNEUROSCI.1660-06.2006
- 903 Pugh, J.R., Jahr, C.E., 2011. Axonal GABAA receptors increase cerebellar granule cell
904 excitability and synaptic activity. *Journal of Neuroscience* 31, 565–574.
905 doi:10.1523/JNEUROSCI.4506-10.2011
- 906 Raimondo, J.V., Kay, L., Ellender, T.J., Akerman, C.J., 2012. Optogenetic silencing strategies
907 differ in their effects on inhibitory synaptic transmission. *Nat Neurosci* 15, 1102–1104.
908 doi:10.1038/nn.3143
- 909 Rivera, J.F., Ahmad, S., Quick, M.W., Liman, E.R., Arnold, D.B., 2003. An evolutionarily
910 conserved dileucine motif in Shal K⁺ channels mediates dendritic targeting. *Nat Neurosci* 6,
911 243–250. doi:10.1038/nn1020
- 912 Robinson, R.B., Siegelbaum, S.A., 2003. Hyperpolarization-activated cation currents: from
913 molecules to physiological function. *Annu. Rev. Physiol.* 65, 453–480.
914 doi:10.1146/annurev.physiol.65.092101.142734
- 915 Rosales, C.R., Osborne, K.D., Zuccarino, G.V., Scheiffele, P., Silverman, M.A., 2005. A
916 cytoplasmic motif targets neuroligin-1 exclusively to dendrites of cultured hippocampal
917 neurons. *The European journal of neuroscience* 22, 2381–2386. doi:10.1111/j.1460-
918 9568.2005.04400.x
- 919 Shemesh, O.A., Tanese, D., Zampini, V., Linghu, C., Piatkevich, K., Ronzitti, E.,
920 Papagiakoumou, E., Boyden, E.S., Emiliani, V., 2017. Temporally precise single-cell-
921 resolution optogenetics. *Nat Neurosci* 20, 1796–1806. doi:10.1038/s41593-017-0018-8
- 922 Stell, B.M., Rostaing, P., Triller, A., Marty, A., 2007. Activation of presynaptic GABA(A)
923 receptors induces glutamate release from parallel fiber synapses. *Journal of Neuroscience* 27,
924 9022–9031. doi:10.1523/JNEUROSCI.1954-07.2007
- 925 Trigo, F.F., Marty, A., Stell, B.M., 2008. Axonal GABAA receptors. *The European journal of*
926 *neuroscience* 28, 841–848. doi:10.1111/j.1460-9568.2008.06404.x
- 927 Turecek, R., Trussell, L.O., 2001. Presynaptic glycine receptors enhance transmitter release at a
928 mammalian central synapse. *Nature* 411, 587–590. doi:10.1038/35079084
- 929 Wietek, J., Beltramo, R., Scanziani, M., Hegemann, P., Oertner, T.G., Simon Wiegert, J., 2015.
930 An improved chloride-conducting channelrhodopsin for light-induced inhibition of neuronal
931 activity in vivo. *Sci Rep* 5, 14807. doi:10.1038/srep14807
- 932 Wietek, J., Wiegert, J.S., Adeishvili, N., Schneider, F., Watanabe, H., Tsunoda, S.P., Vogt, A.,
933 Elstner, M., Oertner, T.G., Hegemann, P., 2014. Conversion of channelrhodopsin into a
934 light-gated chloride channel. *Science* 344, 409–412. doi:10.1126/science.1249375
- 935 Wu, C., Ivanova, E., Zhang, Y., Pan, Z.-H., 2013. rAAV-mediated subcellular targeting of
936 optogenetic tools in retinal ganglion cells in vivo. *PLoS ONE* 8, e66332.
937 doi:10.1371/journal.pone.0066332
- 938 Xia, Y., Zhao, Y., Yang, M., Zeng, S., Shu, Y., 2014. Regulation of action potential waveforms
939 by axonal GABAA receptors in cortical pyramidal neurons. *PLoS ONE* 9, e100968.
940 doi:10.1371/journal.pone.0100968
- 941 Xue, M., Atallah, B.V., Scanziani, M., 2014. Equalizing excitation-inhibition ratios across visual
942 cortical neurons. *Nature* 511, 596–600. doi:10.1038/nature13321
- 943 Zhang, F., Wang, L.-P., Brauner, M., Liewald, J.F., Kay, K., Watzke, N., Wood, P.G., Bamberg,
944 E., Nagel, G., Gottschalk, A., Deisseroth, K., 2007. Multimodal fast optical interrogation of
945 neural circuitry. *Nature* 446, 633–639. doi:10.1038/nature05744
- 946